High-rectification near-field radiative thermal diode using Weyl semimetals

Yang Hu,[1,2,3,*] Haotuo Liu,[3,4,*] Bing Yang,[5] Kezhang Shi,[6] Mauro Antezza,[7,8] Xiaohu Wu,[3,†] and Yasong Sun[1,2,‡]

[1]*Basic Research Center, School of Power and Energy, Northwestern Polytechnical University, Xi'an 710072, Shaanxi, People's Republic of China*

[2]*Center of Computational Physics and Energy Science, Yangtze River Delta Research Institute of NPU, Northwestern Polytechnical University, Taicang 215400, Jiangsu, People's Republic of China*

[3]*Shandong Institute of Advanced Technology, Jinan 250100, Shandong, People's Republic of China*

[4]*School of Energy Science and Engineering, Harbin Institute of Technology, Harbin 150001, People's Republic of China*

[5]*Centre for Advanced Laser Manufacturing (CALM), School of Mechanical Engineering, Shandong University of Technology, Zibo 255000, People's Republic of China*

[6]*Centre for Optical and Electromagnetic Research, National Engineering Research Center for Optical Instruments, Zhejiang University, Hangzhou 310058, People's Republic of China*

[7]*Laboratoire Charles Coulomb (L2C) UMR 5221 CNRS-Université de Montpellier, Montpellier F-34095, France*

[8]*Institut Universitaire de France, 1 Rue Descartes, Paris Cedex 05 F-75231, France*

(Received 4 October 2022; revised 6 December 2022; accepted 24 February 2023; published 13 March 2023)

Thermal diodes, which allow heat transfer in a preferential direction while being blocked in a reverse direction, have numerous applications in thermal management, information processing, energy harvesting, etc. Typical materials of thermal diodes in previous works include phase-change and magneto-optical materials. However, such thermal diodes depend highly on specific working temperatures or external magnetic fields. In this work, we propose a near-field radiative thermal diode (NFRTD) based on two Weyl semimetal (WSM) nanoparticles (NPs) mediated by a WSM planar substrate, which works without an external magnetic field and with flexible temperatures. Numerical results show that the maximum rectification ratio of NFRTD can be up to 2673 when the emitter is 200 K and receiver is 180 K, which exceeds the maximum value reported in some previous works by more than 10 times. The underlying physical mechanism is the strong coupling of the localized plasmon modes in the NPs and nonreciprocal surface plasmon polaritons in the substrate. In addition, we calculate the distribution of the Green's function and reflection coefficient to investigate nonreciprocal energy transfer in NFRTDs. Finally, we discuss the effects of momentum separation on the rectification performance of the NFRTD. This work demonstrates the great potential of WSMs in thermal rectification and paves a path for designing high-performance NFRTDs.

DOI: 10.1103/PhysRevMaterials.7.035201

I. INTRODUCTION

As one of the most important semiconductor devices, the electric diode is not only of great theoretical significance, but also plays an indispensable role in modern industry [1]. Inspired by the effective regulation of electric currents by electric diodes, the manipulation of heat flux has also gradually attracted the research interest of related scientists. Recently, the concept of thermal diodes has been proposed [2–9]. The thermal diodes allow heat to transfer in a forward temperature gradient while being blocked in a reverse temperature gradient [10–13]. Owing to this exotic property of directional control of heat flux, it has potential applications in thermal management, thermal rectification, information processing, and energy harvesting [14–19]. To meet the technical requirements of practical applications, thermal diodes often require a rectification ratio of dozens or even higher. So far, thermal diodes based on various energy carriers (photons, phonons, electrons) have been extensively studied [20–26]. However, the rectification ratio of thermal diodes is still inferior to that of typical electrical diodes, which hinders its application and development in related fields.

Due to the coupling effect of evanescent waves, the near-field radiative heat transfer (NFRHT) may exceed the blackbody limit by several orders of magnitude [27–46]. The radiative heat flux can be effectively modulated based on the near-field effects, paving a path for thermal diodes. Previous works have investigated near-field radiative thermal diode (NFRTD) in a two-body system [2,47–49], in which the thermal rectification ratio is highly temperature dependent. In 2017, Doyeux *et al.* developed energy transfer in the presence of a nonreciprocal object, which suggests that nonreciprocal surface plasmon polaritons (SPPs) can effectively manage energy transport at the nanoscale [50]. Ott *et al.* proposed a NFRTD based on many-body systems [51], in which the NFRHT can be manipulated between nanoparticles (NPs) with nonreciprocity of the magneto-optical materials that depends on the magnetic field. In comparison, the Weyl semimetals (WSMs) can obtain a superior nonreciproc-

*These authors contributed equally to this work.
†Corresponding author: xiaohu.wu@iat.cn
‡Corresponding author: yssun@nwpu.edu.cn

 ©2023 American Physical Society

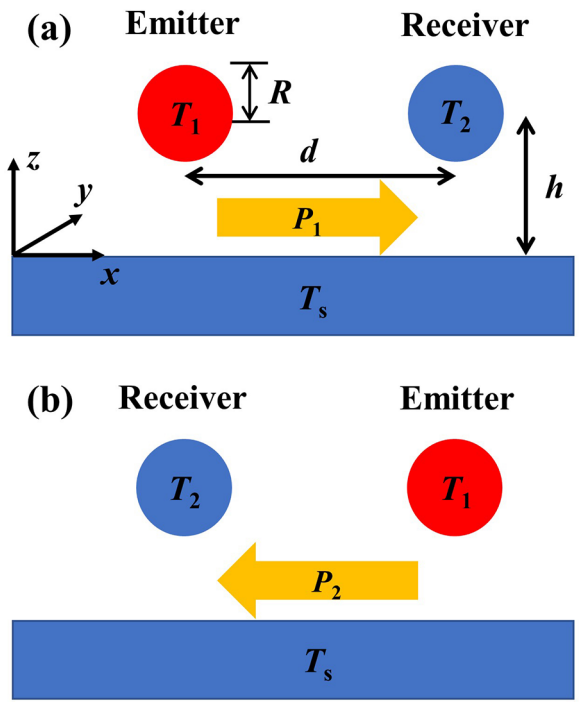

FIG. 1. Schematic diagram of the NFRTD. The two NPs with radius R are placed along the x axis at a gap distance of d and in the vicinity of a WSM substrate at a distance of h. The coordinates of the emitter and receiver are $\mathbf{r}_1$ and $\mathbf{r}_2$. (a) $\mathbf{r}_1 = (0\,0\,h)$, $\mathbf{r_2} = (d\,0\,h)$, and (b) $\mathbf{r}_1 = (d\,0\,h)$, $\mathbf{r}_2 = (0\,0\,h)$. The temperature of the emitter, receiver, and substrate are T_1, T_2, and T_s. The forward and backward heat flux are P_1 and P_2, respectively.

ity without an applied magnetic field [52–61]. In addition, the temperature-dependent optical properties of WSMs offer flexibility for the control of the rectification performance of NFRTDs. To date, the NFRHT between WSMs has been investigated theoretically [62–64]. However, the rectification potential of the NFRTD based on WSMs has not been explored, and the underlying physical mechanisms need to be further discussed.

In this work, we propose a NFRTD using WSMs to achieve a high rectification ratio. The 4×4 transfer matrix method and fluctuational electrodynamics are used to calculate the NFRHT between WSM NPs mediated by a WSM planar substrate [65,66]. Owing to strong coupling of the localized plasmon modes in the NPs and nonreciprocal SPPs in the substrate, we can effectively modulate the rectification performance of the NFRTD. In addition, we discuss the distribution of the Green's function in angular frequency and wave vector space to reveal the underlying physical mechanism. Finally, we investigate the effects of temperature and momentum separation on the rectification performance of the NFRTD. We believe the results in this work can provide guidance for the design of high-performance NFRTDs based on WSMs.

II. MODELING AND CALCULATION

The schematic diagram of the NFRTD, which consists of a WSM planar substrate and two WSM NPs placed above it, is as shown in Fig. 1. The radius R of the WSM NPs is 20 nm. The distance between the NPs and from the NPs to the plate is $d = 1000$ nm and $h = 100$ nm, respectively. The WSM planar substrate is considered as a semi-infinite medium. The temperature of the red particle (emitter), blue particle (receiver), and planar substrate are T_1, T_2, and T_S, respectively. To simplify the computational model, we assume that $T_1 > T_2 = T_S$. A Cartesian coordinate system is established with the projection of the spherical center of the left particle on the upper surface of the WSM planar substrate as the origin. When the emitter is on the left side, we define the NFRHT as forward transfer, and the heat flow is P_1. The coordinates of the emitter and receiver are $\mathbf{r_1} = (0\,0\,h)$ and $\mathbf{r_2} = (d\,0\,h)$. When the emitter is on the right side, the NFRHT is backward transfer, and the heat flow is P_2. The coordinates of the emitter and receiver are $\mathbf{r}_1 = (d\,0\,h)$ and $\mathbf{r_2} = (0\,0\,h)$. By changing the positions of the WSM NPs, we can effectively modulate the NFRHT between two WSM NPs mediated by a WSM planar substrate and obtain a higher theoretical rectification ratio. It is worth noting that the dipole approximation can be nicely adapted when d, h, $\lambda \gg R$, and two NPs can be described as point sources [66,67].

Specifically, we considered the simplest case of WSM. The time-reversal symmetry could be broken when splitting a Dirac point into a pair of Weyl nodes with opposite chirality. Each pair of Weyl nodes is separated in momentum space by wave vector $\mathbf{b}$. This kind of material has been recently realized experimentally, for example, $EuCd_2As_2$. Moreover, the presence of Weyl nodes changes the electromagnetic response, and the displacement electric field for WSM can be written as [52,53]

$$\mathbf{D} = \varepsilon_{\mathrm{d}}\mathbf{E} + \frac{ie^2}{4\pi^2\hbar\omega}(-2b_0\mathbf{B} + 2\mathbf{b} \times \mathbf{E}), \tag{1}$$

where e is the elementary charge, $\hbar$ is the reduced Planck constant, $\mathbf{E}$ is the electric field, $\mathbf{B}$ is the magnetic flux density, and ε_{d} is the permittivity of the corresponding Dirac semimetal. It is worth noting that Dirac semimetals are generally assumed to be isotropic in the absence of external magnetic fields. Thus, we assume that the diagonal elements of the permittivity tensor are all ε_{d}. The first $(-2b_0\mathbf{B})$ and the second $(2\mathbf{b} \times \mathbf{E})$ terms in the parentheses of Eq. (1) describe the chiral magnetic effect and the anomalous Hall effect, respectively. In this work, we only consider materials where the Weyl nodes have the same energy (i.e., $b_0 = 0$). The momentum separation $\mathbf{b}$ of the Weyl nodes is an axial vector that acts similarly to an internal magnetic field, and we choose the coordinates with $\mathbf{b}$ along the positive y direction: (i.e., $\mathbf{b} = b\mathbf{y}$). With the above considerations, the permittivity tensor of the WSM becomes

$$\boldsymbol{\varepsilon} = \begin{bmatrix} \varepsilon_{\mathrm{d}} & 0 & i\varepsilon_{\mathrm{a}} \\ 0 & \varepsilon_{\mathrm{d}} & 0 \\ -i\varepsilon_{\mathrm{a}} & 0 & \varepsilon_{\mathrm{d}} \end{bmatrix}, \tag{2}$$

where

$$\varepsilon_{\mathrm{a}} = \frac{be^2}{2\pi^2\varepsilon_0\hbar\omega}. \tag{3}$$

When $b \neq 0$, ε_{a} is nonzero. Thus, ε is asymmetric and could break Lorentz reciprocity. To calculate the diagonal term ε_{d}, we apply the Kubo Greenwood formalism within the random phase approximation to a two-band model with

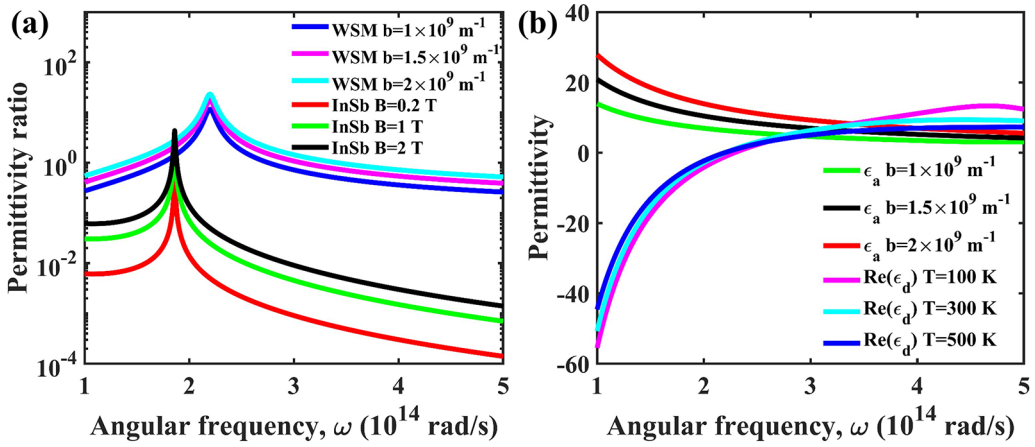

FIG. 2. (a) The permittivity ratio ($|\varepsilon_a/\varepsilon_d|$ for WSMs and $|\varepsilon_1/\varepsilon_2|$ for InSb) varies with angular frequency. The temperature of the WSMs is 300 K. (b) The permittivity tensor components (ε_a and ε_d) of the WSMs vary with angular frequency.

spin degeneracy. This formalism considers both interband and intraband transitions [68,69],

$$\varepsilon_d = \varepsilon_b + i\frac{\sigma}{\omega}, \tag{4}$$

where σ is the bulk conductivity given by

$$\sigma = \frac{r_s g}{6}\Omega G\left(\frac{\Omega}{2}\right) + i\frac{r_s g}{6\pi}\left(\frac{4}{\Omega}\left\{1+\frac{\pi^2}{3}\left[\frac{k_B T}{E_F(T)}\right]^2\right\} + 8\Omega\int_0^{\xi_c}\frac{G(\xi)-G\left(\frac{\Omega}{2}\right)}{\Omega^2-4\xi^2}\xi d\xi\right), \tag{5}$$

where ε_b is the background permittivity, $\Omega = \hbar(\omega + i\tau^{-1})/E_F$ is the complex frequency normalized by the chemical potential, τ^{-1} is the scattering rate corresponding to Drude damping, $G(E) = n(-E) - n(E)$ where $n(E)$ is the Fermi distribution function, $E_F(T)$ is the chemical potential, $r_s = e^2/4\pi\varepsilon_0\hbar v_F$ is the effective fine structure constant, v_F is the Fermi velocity, g is the number of Weyl points, and $\xi_c = E_c/E_F$ where E_c is the cutoff energy beyond which the band dispersion is nonlinear. Other important parameters are as follows: $\varepsilon_b = 6.2$, $\xi_c = 3$, $\tau = 1000$ fs, $g = 2$, and $v_F = 0.83 \times 10^9$ m/s. The chemical potential as a function of temperature can be calculated from charge conservation [52]:

$$E_F(T) = \frac{2^{1/3}\left[9E_F(0)^3 + \sqrt{81E_F(0)^6 + 12\pi^6 k_B^6 T^6}\right]^{2/3} - 2\pi^2 3^{1/3} k_B^2 T^2}{6^{2/3}\left[9E_F(0)^3 + \sqrt{81E_F(0)^6 + 12\pi^6 k_B^6 T^6}\right]^{1/3}}, \tag{6}$$

where $E_F\,(0\,\mathrm{K}) = 0.163$ eV and $E_F(300\,\mathrm{K}) = 0.150$ eV.

The permittivity of magneto-optical material InSb is given by [70]

$$\boldsymbol{\varepsilon} = \begin{bmatrix} \varepsilon_1 & 0 & i\varepsilon_2 \\ 0 & \varepsilon_3 & 0 \\ -i\varepsilon_2 & 0 & \varepsilon_1 \end{bmatrix}. \tag{7}$$

Note that the direction of the magnetic field is in the positive y direction. The detailed calculation parameters can be found in Ref. [71].

The permittivity ratio represents the ratio of the nondiagonal elements to the main diagonal elements in the permittivity tensor, which is an effective parameter to describe the performance of nonreciprocal materials [69]. To compare the nonreciprocity of the two materials, we define the permittivity ratio: $|\varepsilon_a/\varepsilon_d|$ for WSMs and $|\varepsilon_1/\varepsilon_2|$ for InSb. Figure 2(a) shows the permittivity ratio of the WSMs and Insb as a function of angular frequency. Note that the temperature of the WSMs is 300 K. The off-diagonal elements of the WSMs and InSb are determined by momentum separation b and magnetic field, respectively. It can be seen that even when InSb is under a very strong magnetic field (∼2 T), its nonreciprocity is still inferior to that of WSMs. This is due to the separation of the Weyl nodes in momentum separation b having relatively large values for compounds such as $EuCd_2As_2$. In addition, the strong nonreciprocity of WSMs can be obtained without an applied magnetic field, which is its significant advantage over the magneto-optical material InSb. We further calculated the WSM permittivity tensor components (ε_a and ε_d) versus angular frequency, as shown in Fig. 2(b). We find that ε_a is comparable to ε_d over the entire display wavelength range. In addition, ε_a and ε_d are strongly correlated with the momentum separation and temperature, respectively, which provides us with more possibilities for the nonreciprocal regulation of WSMs.

The total heat flux received by NP_i can be described as [51]

$$P_i = \int_0^\infty \frac{d\omega}{2\pi}P_{i,\omega} = 3\int_0^\infty \frac{d\omega}{2\pi}[\Theta(T_j) - \Theta(T_i)]\tau_{ji}, \tag{8}$$

where $\Theta(T) = \hbar\omega/[\exp(\hbar\omega/k_B T) - 1]$ is the mean energy of the Planck thermal harmonic oscillators, and $\tau_{ji} = 4k_0^4 \mathrm{Tr}[\boldsymbol{\chi}_i \mathbf{G}_{ij} \boldsymbol{\chi}_j \mathbf{G}_{ij}^*]/3$ is the transmission coefficient for the heat flux between the NPs [72,73]. Here "*" denotes the conjugate transpose. $\boldsymbol{\chi}_i = (\boldsymbol{\alpha}_i - \boldsymbol{\alpha}_i^*)/2i$ is the dressed polarizability of NP$_i$ [67,72]. When ignoring radiative correction, the polarizability of an anisotropic NP could be written in Clausius-Mossotti form [32,74]. For dielectric NPs, the magnetic polarizability can be ignored. When the NP is surrounded by vacuum, the electric polarizability of the anisotropic NPs $\boldsymbol{\alpha}_i$ is given as [32]

$$\boldsymbol{\alpha}_i = 4\pi R^3 \frac{\boldsymbol{\varepsilon}_i - 1\mathbf{I}}{\boldsymbol{\varepsilon}_i + 2\mathbf{I}}, \tag{9}$$

where $\mathbf{I}$ is the unit matrix and $\boldsymbol{\varepsilon}_1$ ($\boldsymbol{\varepsilon}_2$) is the permittivity tensor of the emitter (receiver). $\mathbf{G}_{ij}$ in τ_{ji} is the dyadic Green's tensor:

$$\mathbf{G}_{ij} = \mathbf{G}_{ij}^{(0)} + \mathbf{G}_{ij}^{(sc)}, \tag{10}$$

where $\mathbf{G}_{ij}^{(0)}$ is the vacuum Green's function, which is related to the position of the NPs [75],

$$\mathbf{G}_{ij}^{(0)} = \mathbf{G}^{(0)}(\mathbf{r}_i, \mathbf{r}_j) = \frac{e^{ik_0 r_{ij}}}{4\pi r_{ij}} \left[\left(1 + \frac{ik_0 r_{ij} - 1}{k_0^2 r_{ij}^2}\right)\mathbf{I} + \frac{3 - 3ik_0 r_{ij} - k_0^2 r_{ij}^2}{k_0^2 r_{ij}^2} \hat{\mathbf{r}}_{ij} \otimes \hat{\mathbf{r}}_{ij} \right], \tag{11}$$

where k_0 is the vacuum wave vector, $r_{ij} = |\mathbf{r}_{ij}|$ is the magnitude of the vector linking two NPs, $\hat{\mathbf{r}}_{ij} = \mathbf{r}_{ij}/r_{ij}$, and $\otimes$ is the outer product.

$$\mathbf{G}_{ij}^{(sc)} = \frac{i}{8\pi^2} \int_{-\infty}^{\infty} dk_x \times \int_{-\infty}^{\infty} \left(r_{ss}\mathbf{M}_{ss} + r_{ps}\mathbf{M}_{ps} + r_{sp}\mathbf{M}_{sp} + r_{pp}\mathbf{M}_{pp}\right) \times e^{i[k_x(x_i - x_j) + k_y(y_i - y_j)]} e^{ik_z|z_i + z_j|} dk_y, \tag{12}$$

where $\mathbf{G}_{ij}^{(sc)}$ is the scatter Green's function, which is associated with substrate presence [76]. r is the reflection coefficient related to incident "s" and "p" polarized waves. k_x and k_y are the in-plane wave vectors, and k_z is the out of plane wave vector.

$$\mathbf{M}_{ss} = \frac{1}{k_z k_\rho^2} \begin{pmatrix} k_y^2 & -k_x k_y & 0 \\ -k_x k_y & k_x^2 & 0 \\ 0 & 0 & 0 \end{pmatrix},$$

$$\mathbf{M}_{pp} = \frac{k_z}{k_0^2 k_\rho^2} \begin{pmatrix} -k_x^2 & -k_x k_y & -k_x k_\rho^2/k_z \\ -k_x k_y & -k_y^2 & -k_y k_\rho^2/k_z \\ k_x k_\rho^2/k_z & k_y k_\rho^2/k_z & k_\rho^4/k_z^2 \end{pmatrix},$$

$$\mathbf{M}_{sp} = \frac{1}{k_0 k_\rho^2} \begin{pmatrix} -k_x k_y & -k_y^2 & -k_y k_\rho^2/k_z \\ k_x^2 & k_x k_y & k_x k_\rho^2/k_z \\ 0 & 0 & 0 \end{pmatrix},$$

$$\mathbf{M}_{ps} = \frac{1}{k_0 k_\rho^2} \begin{pmatrix} k_x k_y & -k_x^2 & 0 \\ k_y^2 & -k_x k_y & 0 \\ -k_y k_\rho^2/k_z & k_x k_\rho^2/k_z & 0 \end{pmatrix}. \tag{13}$$

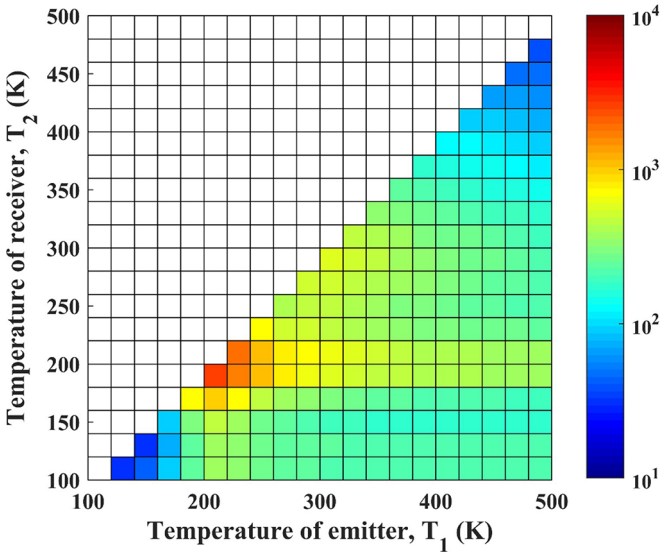

FIG. 3. The rectification ratio varies with the temperature of the emitter T_1 and the temperature of the receiver T_2. The temperature of the planar substrate is $T_S = T_2$. The momentum separation is $b = 2 \times 10^9\ \mathrm{m}^{-1}$.

III. RESULTS AND DISCUSSION

To quantitatively describe the performance of the NFRTD, we define the rectification ratio as the ratio of the difference between the forward and backward total heat flux to the minimum total heat flux [49,77]:

$$\eta = \frac{P_2 - P_1}{P_1}. \tag{14}$$

Figure 3 gives the relationship of the rectification ratio to the temperature of the emitter (T_1) and receiver (T_2), where $T_1 > T_2$. The temperature of the planar substrate is equal to that of the receiver, i.e., $T_2 = T_S$. The momentum separation b is set to $2 \times 10^9\ \mathrm{m}^{-1}$. We found that the rectification ratio strongly depends on the temperature with WSM NPs. When $T_1 = 200$ K and $T_2 = 180$ K, we can obtain a rectification ratio of 2673, which exceeds the maximum rectification ratio of some previous works by more than a factor of 10 [51,71,76,78]. The low-temperature thermal diodes have applications in deep and low-temperature heat harvesting and heat transfer technology [79–81]. This may be due to the effect of temperature on the nonreciprocity of the WSMs, resulting in a significant difference between the forward and backward heat flux. In addition, it could achieve a high rectification ratio at a smaller temperature difference compared to conventional NFRTD.

To understand the high rectification ratio, we calculated the forward transmission coefficient T_{12} and backward transmission coefficient T_{21} between WSM NPs. As shown in Fig. 4(a), three resonances occur at 1.35×10^{14}, 2.1×10^{14}, and 3.1×10^{14} rad/s for both T_{12} and T_{21}. The enhancement of NFRHT is related to the coupling of threefold degenerate localized modes in NPs and the surface modes in the substrate. The frequencies of localized plasmon modes $\omega_{m=0,\pm1}$ corresponding to quantum number $m = 0, \pm1$ is determined

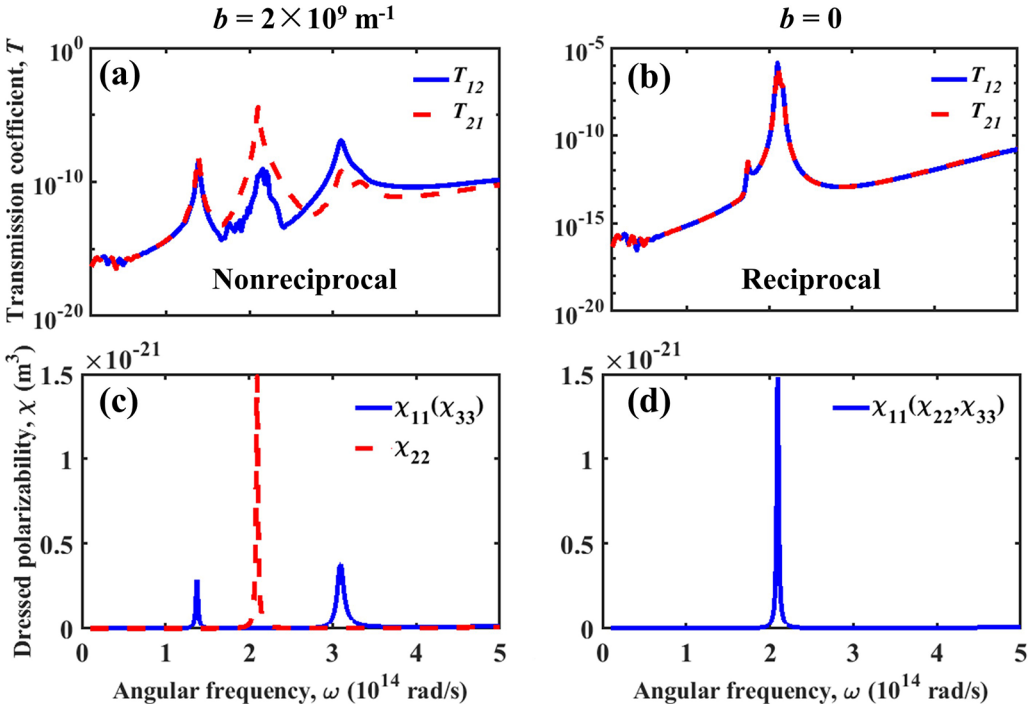

FIG. 4. The forward transmission coefficient T_{12} and backward transmission coefficient T_{21} between WSM NPs for the momentum separation of (a) $b = 2 \times 10^9\ \mathrm{m}^{-1}$ and (b) $b = 0$. The temperature of the emitter and receiver is $T_1 = 200$ K and $T_2 = 180$ K. The dressed polarizability of WSM NPs at temperature of 200 K for the momentum separation of (c) $b = 2 \times 10^9\ \mathrm{m}^{-1}$ and (d) $b = 0$.

by dressed polarizability, which can be expressed as [82]

$$\boldsymbol{\chi}_i = \begin{pmatrix} \chi_{11} & 0 & \chi_{13} \\ 0 & \chi_{22} & 0 \\ \chi_{31} & 0 & \chi_{33} \end{pmatrix}, \tag{15}$$

where $\chi_{11} = \chi_{33}$, and $\chi_{13} = -\chi_{31}$. The resonance frequency of the WSM NPs can be determined by [83–85]

$$\det\left[\boldsymbol{\varepsilon}(\omega, T) + 2\mathbf{I}\right] = (\varepsilon_\mathrm{d} + 2)\left[(\varepsilon_\mathrm{d} + 2)^2 - \varepsilon_\mathrm{a}^2\right] = 0. \tag{16}$$

Thus, the resonance modes appear when $(\varepsilon_\mathrm{d} + 2) = 0$ or $(\varepsilon_\mathrm{d} + 2)^2 - \varepsilon_\mathrm{a}^2 = 0$. For the NFRHT between WSM NPs, the main diagonal component of the dressed polarizability tensor dominates. Next, we mainly analyzed these three components. The resonance of 1.35×10^{14}, 2.1×10^{14}, and 3.1×10^{14} rad/s corresponds to χ_{11}, χ_{22}, and χ_{33}, respectively. The resonance of 2.1×10^{14} rad/s depends on the localized plasmon mode of $(\varepsilon_\mathrm{d} + 2) = 0$; thus it is strongly related to the temperature of WSM NPs. This momentum separation independent mode is the "nonrotating" mode that exhibits zero angular momentum ($m = 0$). The T_{12} is several orders of magnitude lower than T_{21}, demonstrating strong nonreciprocity due to the temperature difference of WSM NPs. The resonance of 1.35×10^{14}, and 3.1×10^{14} rad/s depends on the localized circular mode of $(\varepsilon_\mathrm{d} + 2)^2 - \varepsilon_\mathrm{a}^2 = 0$; thus it is related to both temperature and momentum separation of WSM NPs. The resonance at an angular frequency of 3.1×10^{14} rad/s for the heat flux rotates clockwise along the momentum separation ($m = -1$). The T_{12} and T_{21} are equal, and there is no nonreciprocity. The resonance at an angular frequency of 1.35×10^{14} rad/s for the heat flux rotates counterclockwise along the momentum separation ($m = +1$). The T_{12} is a little larger than T_{21}, exhibiting weaker nonreciprocity. Figures 4(b) and 4(d) give the spectral heat flux and dressed polarizability of WSM NPs for the momentum separation of $b = 0$. Only the localized plasmon modes are excited, and the NFRHT between the WSM NPs becomes strictly reciprocal in this case. Moreover, the polarizability tensor has only equal main diagonal elements.

To explain the heat transfer mechanism, the Green's function for the forward and backward heat flux varying with angular frequency is investigated (Fig. 5). Since the nonreciprocal effect of this system depends mainly on the substrate, the polarizability effect on the Green's function is not considered. Equation (10) indicates that Green's function $\mathbf{G}$ consists of a vacuum function $\mathbf{G}^{(0)}$ and a scattering function $\mathbf{G}^{(\mathrm{sc})}$. The Green's function in the transmission coefficient can be decomposed into three parts:

$$\begin{aligned}\mathrm{Tr}(\mathbf{G}\mathbf{G}^*) = {} & \mathrm{Tr}(\mathbf{G}^{(\mathbf{0})}\mathbf{G}^{(\mathbf{0})*}) + \mathrm{Tr}(\mathbf{G}^{(\mathbf{sc})}\mathbf{G}^{(\mathbf{sc})*}) \\ & + 2\mathrm{Tr}(\boldsymbol{\chi}\mathbf{G}^{(\mathbf{0})}\boldsymbol{\chi}\mathbf{G}^{(\mathbf{sc})*}).\end{aligned} \tag{17}$$

The right side of Eq. (17) represents the sum of vacuum, scattering, and cross contributions [86], respectively. The scattering and cross contribution are associated with the presence of the substrate. The $\mathbf{G}^{(\mathrm{sc,sc})}$ agrees well with the $\mathbf{G}$, representing that the NFRHT is mainly through the substrate rather than vacuum. When $b = 0$, the Green's function varies with different angular frequencies [Fig. 5(a)]. The total Green's function (black line) has only a resonance at the angular frequency of 2.17×10^{14} rad/s. At this angular frequency, the contribution of the total Green function is mainly by the substrate, and the frequency corresponds to the position where $\mathrm{Re}(\varepsilon_\mathrm{d})$ is -1, indicating the excitation of surface modes in the substrate

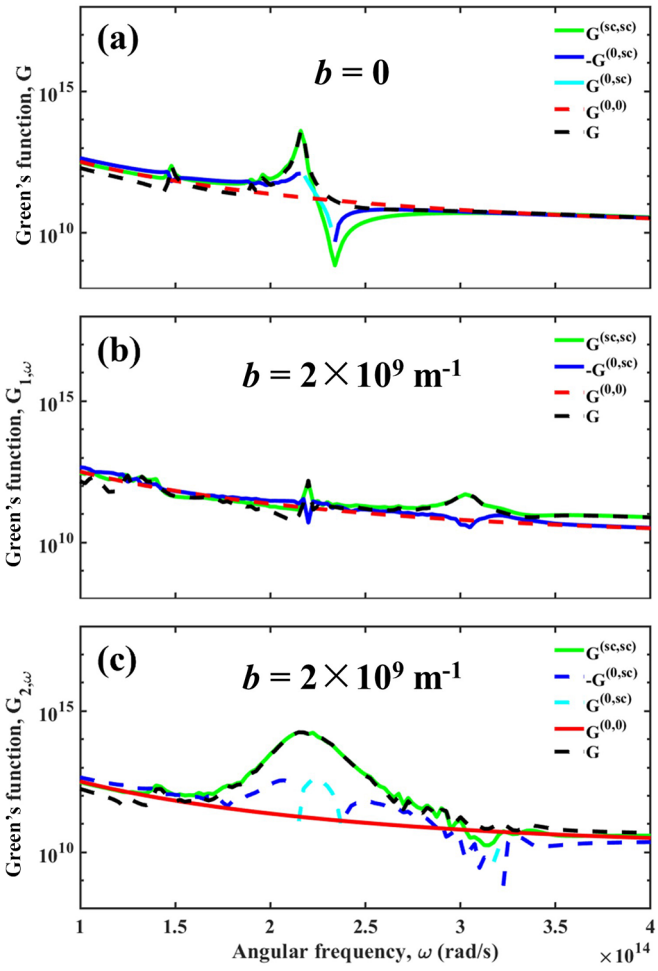

FIG. 5. The Green's function varies with angular frequency. Green lines represent the scattering contribution, blue lines represent the negative cross contribution, cyan lines represent the positive cross contribution, red lines represent the vacuum contribution, and black lines represent the total contribution. (a) $b = 0$, (b) $b = 2 \times 10^9\ \mathrm{m}^{-1}$ corresponding to P_1, and (c) $b = 2 \times 10^9\ \mathrm{m}^{-1}$ corresponding to P_2.

enhances the NFRHT, while when $b = 2 \times 10^9\ \mathrm{m}^{-1}$, the NFRHT has nonreciprocity, and the Green's functions $\mathrm{G}_{1,\omega}$ and $\mathrm{G}_{2,\omega}$ corresponding to P_1 and P_2 are shown in Figs. 5(b) and 5(c), respectively. For $b = 2 \times 10^9\ \mathrm{m}^{-1}$, three different resonances occur at 2.17×10^{14}, 1.4×10^{14}, and 3.02×10^{14} rad/s due to the nonzero off-diagonal permittivity elements. The resonance at 1.4×10^{14} rad/s is small and has a negligible effect on the total Green's function. The resonance at 2.17×10^{14} rad/s in $\mathrm{G}_{1,\omega}$ is much smaller than that in $\mathrm{G}_{2,\omega}$, as affected by the substrate. Therefore, the directional nonreciprocal surface modes in the substrate leading to the spectral heat flux in $P_{1,\omega}$ are smaller than $P_{2,\omega}$. At the frequency of 3.02×10^{14} rad/s, the $\mathrm{G}_{1,\omega}$ is larger than $\mathrm{G}_{2,\omega}$, corresponding to $P_{1,\omega}$ being larger than $P_{2,\omega}$. The mechanism is also due to the excitation of nonreciprocal surface modes, while the nonreciprocal effect is weaker.

Further, we calculate the distribution of the scattering Green's function in the wave vector space to obtain an intuitive understanding of the influence of the substrate on the nonreciprocal energy transfer, as shown in Fig. 6. When $b = 0$, the scattering Green's function is consistent on the forward and backward heat flux; thus there is no nonreciprocal effect in the near-field thermal diode [Figs. 6(a) and 6(b)]. When the momentum separation $b = 2 \times 10^9\ \mathrm{m}^{-1}$, the symmetry of eigenstates with positive and negative k_x is damaged by the momentum separation, leading to a strong nonreciprocal surface mode in the substrate. When the angular frequency $\omega = 1.35 \times 10^{14}$ rad/s, the forward and reverse heat fluxes are almost equal. Therefore, it can be considered that the NFRTDs are reciprocal, which reflects good agreement with Fig. 4(a). When the angular frequency $\omega = 2.1 \times 10^{14}$ rad/s, the distribution of the scattering Green's function in positive and negative k_x space has an asymmetrical character. Specifically, the narrow blue bright band at the positive k_x space shifts to red from Figs. 6(e) to 6(f), which significantly enhances the radiative heat flux P_2, producing a strong nonreciprocity. When the angular frequency $\omega = 3.1 \times 10^{14}$ rad/s, the distribution of the scattering Green's function in negative k_x space is slightly different in Figs. 6(g) and 6(h), leading to smaller nonreciprocity.

To explain the mechanism of the asymmetric distribution of Green's functions at different resonance frequencies, the imaginary part of r_{pp} is shown in Fig. 7. The double "p" in the subscript of r_{pp} indicates the incoming p-polarized wave and reflected p-polarized wave, respectively. The imaginary part of r_{pp} is proportional to the density of states of the photons, and the near-field coupling of the two WSM NPs via the nonreciprocal SPPs of the substrate is mainly given by the component r_{pp} of the reflection tensor $\begin{pmatrix} r_{pp} & r_{ps} \\ r_{sp} & r_{ss} \end{pmatrix}$ [71,87]. Thus, we can understand the underlying physical mechanisms by focusing on the component r_{pp}. When the momentum separation $\mathbf{b} = 0$, the WSM substrate supports isotropic surface modes because there is no off-diagonal component in the permittivity tensor, while when the momentum separation $b = 2 \times 10^9\ \mathrm{m}^{-1}$, the momentum separation is along the positive y direction, and the reflection coefficient shows asymmetry in positive and negative k_x spaces. At an angular frequency of 1.35×10^{14} rad/s, the value of the reflection coefficient is small, and the nonreciprocal effect is weak [Fig. 7(b)]. However, Fig. 7(c) shows two narrow bright bands in positive k_x space at an angular frequency of 2.1×10^{14} rad/s, leading to a strong nonreciprocal effect. When the angular frequency $\omega = 3.1 \times 10^{14}$ rad/s, the reflection coefficient has a wide bright band but a small value, resulting in a weak nonreciprocal effect.

Our study is not limited to a specific material, but a class of materials with different momentum separations. We further investigate the rectification ratio η versus momentum separation $\mathbf{b}$ and give the corresponding permittivity ratio $|\varepsilon_\mathrm{a}/\varepsilon_\mathrm{d}|$ to discuss the performance of the NFRTD, as shown in Fig. 8. The temperature of emitter and receiver is $T_1 = 200$ K and $T_2 = 180$ K, respectively. The rectification ratio η fluctuates upward with the increase of momentum separation. The permittivity ratio $|\varepsilon_\mathrm{a}/\varepsilon_\mathrm{d}|$ increases with increasing momentum separation at the resonance frequency of localized plasmon modes $\omega = 2.1 \times 10^{14}$ rad/s when the temperature is 200 K. Therefore, the nonreciprocal effect of the NFRTD was enhanced, leading to a higher rectification ratio. When the momentum separation $b = 2 \times 10^9\ \mathrm{m}^{-1}$, the rectification ratio

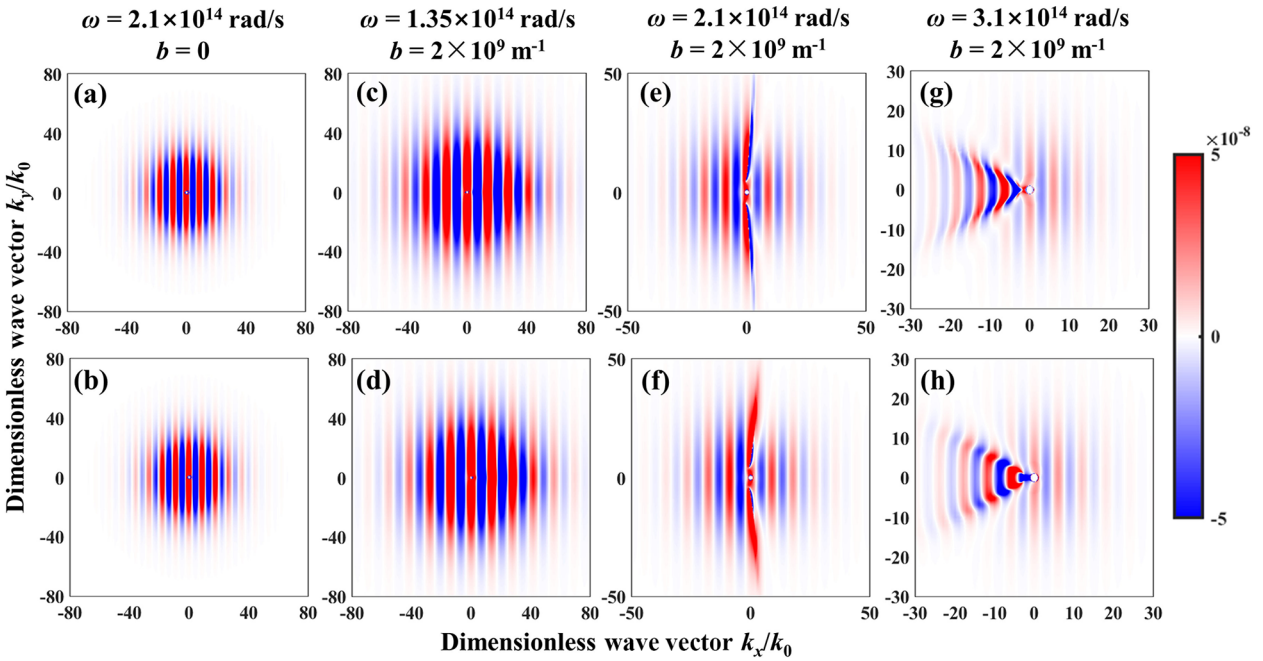

FIG. 6. The real part of $G^{(sc)}(3, 3)$ varies with dimensionless wave vector components k_x and k_y for different angular frequencies and momentum separations: (a), (b) $\omega = 2.1 \times 10^{14}$ rad/s, $b = 0$; (c), (d) $\omega = 1.35 \times 10^{14}$ rad/s, $b = 2 \times 10^9$ m^{-1}; (e), (f) $\omega = 2.1 \times 10^{14}$ rad/s, $b = 2 \times 10^9$ m^{-1}; and (g), (h) $\omega = 3.1 \times 10^{14}$ rad/s, $b = 2 \times 10^9$ m^{-1}. The first row corresponds to $P_{1,\omega}$, and the second row corresponds to $P_{2,\omega}$.

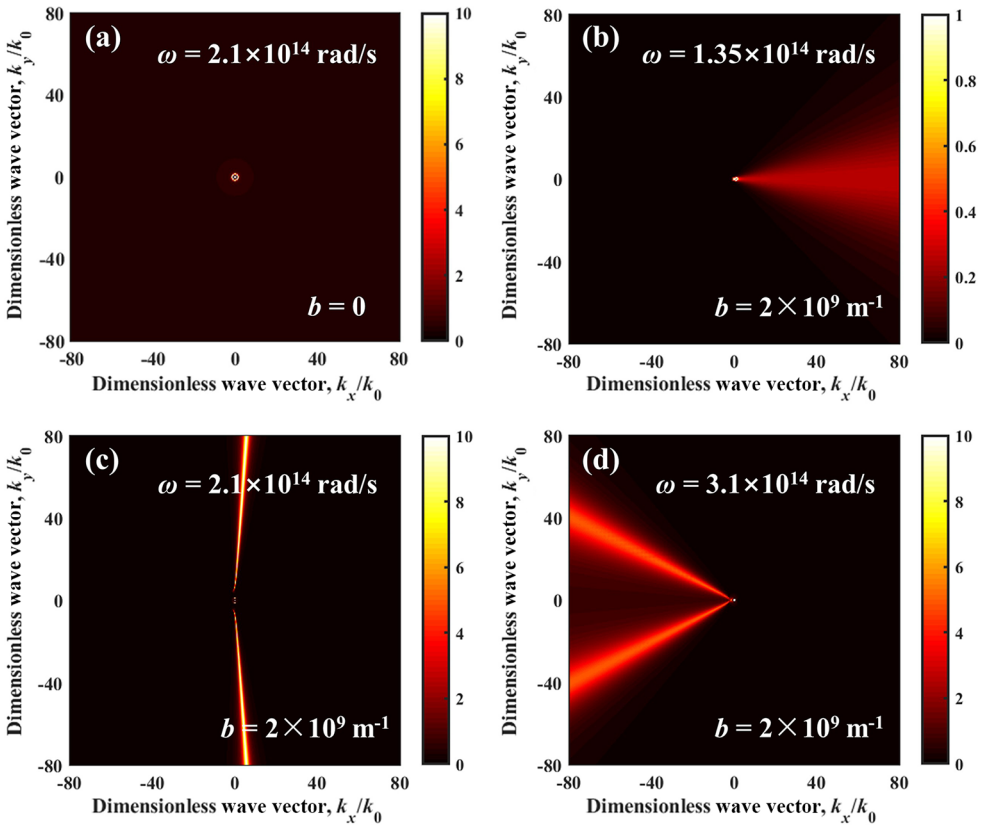

FIG. 7. The imaginary part of r_{pp} varies with wave vector components k_x and k_y for different angular frequencies and momentum separations: (a) $\omega = 1.35 \times 10^{14}$ rad/s, $b = 0$; (b) $\omega = 1.35 \times 10^{14}$ rad/s, $b = 2 \times 10^9$ m^{-1}; (c) $\omega = 2.1 \times 10^{14}$ rad/s, $b = 2 \times 10^9$ m^{-1}; and (d) $\omega = 3.1 \times 10^{14}$ rad/s, $b = 2 \times 10^9$ m^{-1}.

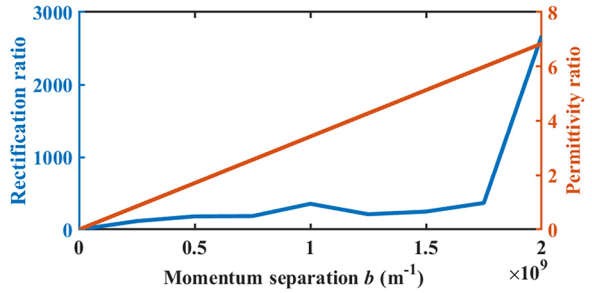

FIG. 8. Left: the rectification ratio η varying with momentum separation. The temperature of the emitter is 200 K, and the temperature of the receiver is 180 K. Right: permittivity ratio $|\varepsilon_a/\varepsilon_d|$ varying with momentum separation when the temperature is 200 K, and angular frequency is $\omega = 2.1 \times 10^{14}$ rad/s.

can reach 2673. So far, the rectification ratio is ∼249 for InSb NPs mediated by an InSb substrate, and ∼88.67 for SiC NPs mediated by drift-biased graphene grating [71,78]. The strong rectification of conventional thermal diodes, such as intrinsic semiconductors or the vanadium dioxide based rectification method, occurs only close to the critical temperature of these materials. Furthermore, obtaining a good rectification effect often requires a large temperature difference, which is difficult to implement experimentally. In contrast, a WSM-based near-field radiative diode could get a high rectification ratio in a small temperature difference. In addition, the rectification effect varies with the emitter and receiver and could change with the parameters of WSM, such as the number of Weyl points g, the Fermi velocity v_F, the background permittivity ε_b, and the scattering rate corresponding to Drude damping τ.

Our findings can provide theoretical guidance for multiprobe-based near-field thermal radiation systems similar to the model of Ben-Abdallah [88]. A direct measurement of the rectification effect might be possible with a many-body heat transfer setup like that developed by Reddy's group, which seems to be feasible [89]. There may be other possibilities, but since our work is biased toward theoretical analysis, it is necessary to explore more details and make further speculations before we move toward experiments.

IV. CONCLUSION

In summary, we theoretically investigate a NFRTD that consists of two WSM NPs mediated by a WSM planar substrate. Due to the strong coupling of the localized plasmon modes in the NPs and nonreciprocal SPPs in the substrate, the maximum rectification ratio of NFRTD can be up to 2673, which exceeds the maximum value reported in some previous works over 10 times. The contributions of the vacuum, scattering, and cross terms under the influence of WSM NPs are investigated to explore the underlying mechanism of the high rectification ratio. Moreover, we calculate the distribution of the Green's function and reflection coefficient to investigate nonreciprocal energy transfer in NFRTD. Finally, we investigate the effects of temperature and momentum separation on the rectification performance of the NFRTD. We believe that this work can be helpful for the design of high-performance NFRTD and facilitate the application of WSMs in thermal rectification.

ACKNOWLEDGMENTS

This work is supported by the National Natural Science Foundation of China (Grants No. 52106099 and No. 51976173), the Shandong Provincial Natural Science Foundation (Grant No. ZR2022YQ57), the Taishan Scholars Program, the Jiangsu Provincial Natural Science Foundation (Grant No. BK20201204), the Basic Research Program of Taicang (Grant No. TC2019JC01), and the Fundamental Research Funds for the Central Universities (Grant No. D5000210779).

[1] N. Li, J. Ren, L. Wang, G. Zhang, P. Hänggi, and B. Li, Colloquium: Phononics: Manipulating heat flow with electronic analogs and beyond, Rev. Mod. Phys. **84**, 1045 (2012).

[2] S. Basu and M. Francoeur, Near-field radiative transfer based thermal rectification using doped silicon, Appl. Phys. Lett. **98**, 113106 (2011).

[3] A. Fiorino, D. Thompson, L. Zhu, R. Mittapally, S. A. Biehs, O. Bezencenet, N. El-Bondry, S. Bansropun, P. Ben-Abdallah, and E. Meyhofer, A thermal diode based on nanoscale thermal radiation, ACS Nano **12**, 5774 (2018).

[4] A. Ghanekar, J. Ji, and Y. Zheng, High-rectification near-field thermal diode using phase change periodic nanostructure, Appl. Phys. Lett. **109**, 123106 (2016).

[5] J. Huang, Q. Li, Z. H. Zheng, and Y. M. Xuan, Thermal rectification based on thermochromic materials, Int. J. Heat Mass Transfer **67**, 575 (2013).

[6] A. Pugsley, A. Zacharopoulos, J. Mondol, and M. Smyth, Theoretical and experimental analysis of a horizontal planar liquid-vapour thermal diode (PLVTD), Int. J. Heat Mass Transfer **144**, 118660 (2019).

[7] J. D. Shen, X. L. Liu, H. He, W. T. Wu, and B. A. Liu, High-performance noncontact thermal diode via asymmetric nanostructures, J. Quant. Spectrosc. Radiat. Transfer **211**, 1 (2018).

[8] L. P. Wang and Z. M. Zhang, Thermal rectification enabled by near-field radiative heat transfer between intrinsic silicon and a dissimilar material, Nanoscale Microscale Thermophys. Eng. **17**, 337 (2013).

[9] Y. Yang, S. Basu, and L. P. Wang, Vacuum thermal switch made of phase transition materials considering thin film and substrate effects, J. Quant. Spectrosc. Radiat. Transfer **158**, 69 (2015).

[10] C. R. Otey, W. T. Lau, and S. H. Fan, Thermal Rectification through Vacuum, Phys. Rev. Lett. **104**, 154301 (2010).

[11] L. X. Zhu, C. R. Otey, and S. H. Fan, Ultrahigh-contrast and large-bandwidth thermal rectification in near-field electromagnetic thermal transfer between nanoparticles, Phys. Rev. B **88**, 184301 (2013).

[12] Q. Z. Li, H. Y. He, Q. Chen, and B. Song, Thin-Film Radiative Thermal Diode with Large Rectification, Phys. Rev. Appl. **16**, 014069 (2021).

[13] Q. Li, H. He, Q. Chen, and B. Song, Radiative Thermal Diode via Hyperbolic Metamaterials, Phys. Rev. Appl. **16**, 064022 (2021).

[14] T. Villeneuve, M. Boudreau, and G. Dumas, The thermal diode and insulating potentials of a vertical stack of parallelogrammic air-filled enclosures, Int. J. Heat Mass Transfer **108**, 2060 (2017).

[15] O. Ilic, N. Thomas, T. Christensen, M. Sherrott, M. Soljacic, A. Minnich, O. Miller, and H. Atwater, Active radiative thermal switching with graphene plasmon resonators, ACS Nano **12**, 2474 (2018).

[16] B. W. Li, L. Wang, and G. Casati, Thermal Diode: Rectification of Heat Flux, Phys. Rev. Lett. **93**, 184301 (2004).

[17] N. Roberts and D. Walker, A review of thermal rectification observations and models in solid materials, Int. J. Therm. Sci. **50**, 648 (2011).

[18] L. Wang and B. Li, Thermal Logic Gates: Computation with Phonons, Phys. Rev. Lett. **99**, 177208 (2007).

[19] T. Ruokola, T. Ojanen, and A. Jauho, Thermal rectification in nonlinear quantum circuits, Phys. Rev. B **79**, 144306 (2009).

[20] Y. Wang, A. Vallabhaneni, J. N. Hu, B. Qiu, Y. P. Chen, and X. L. Ruan, Phonon lateral confinement enables thermal rectification in asymmetric single-material nanostructures, Nano Lett. **14**, 592 (2014).

[21] H. D. Wang, S. Q. Hu, K. Takahashi, X. Zhang, H. Takamatsu, and J. Chen, Experimental study of thermal rectification in suspended monolayer graphene, Nat. Commun. **8**, 1 (2017).

[22] M. Kasprzak, M. Sledzinska, K. Zaleski, I. Iatsunskyi, F. Alzina, S. Volz, C. Torres, and B. Graczykowski, High-temperature silicon thermal diode and switch, Nano Energy **78**, 105261 (2020).

[23] R. Scheibner, M. König, D. Reuter, A. Wieck, C. Gould, H. Buhmann, and L. Molenkamp, Quantum dot as thermal rectifier, New J. Phys. **10**, 083016 (2008).

[24] M. Martínez-Pérez, A. Fornieri, and F. Giazotto, Rectification of electronic heat current by a hybrid thermal diode, Nat. Nanotechnol. **10**, 303 (2015).

[25] E. Nefzaoui, K. Joulain, J. Drevillon, and Y. Ezzahri, Radiative thermal rectification using superconducting materials, Appl. Phys. Lett. **104**, 103905 (2014).

[26] I. Latella, P. Ben-Abdallah, and M. Nikbakht, Radiative thermal rectification in many-body systems, Phys. Rev. B **104**, 045410 (2021).

[27] X. H. Wu, C. J. Fu, and Z. M. Zhang, Near-field radiative heat transfer between two α-MoO_3 biaxial crystals, J. Heat Transfer **142**, 072802 (2020).

[28] X. H. Wu and C. J. Fu, Near-field radiative heat transfer between uniaxial hyperbolic media: Role of volume and surface phonon polaritons, J. Quant. Spectrosc. Radiat. Transfer **258**, 107337 (2021).

[29] X. H. Wu and C. J. Fu, Near-field radiative modulator based on dissimilar hyperbolic materials with in-plane anisotropy, Int. J. Heat Mass Transfer **168**, 120908 (2021).

[30] R. Y. Liu, C. L. Zhou, Y. Zhang, Z. Cui, X. H. Wu, and H. L. Yi, Near-field radiative heat transfer in hyperbolic materials, Int. J. Extreme Manuf. **4**, 032002 (2022).

[31] Y. Hu, Y. S. Sun, Z. H. Zheng, J. L. Song, K. Z. Shi, and X. H. Wu, Rotation-induced significant modulation of near-field radiative heat transfer between hyperbolic nanoparticles, Int. J. Heat Mass Transfer **189**, 122666 (2022).

[32] J. Dong, W. J. Zhang, and L. H. Liu, Nonreciprocal thermal radiation of nanoparticles via spin-directional coupling with reciprocal surface modes, Appl. Phys. Lett. **119**, 021104 (2021).

[33] M. G. Luo, J. Dong, J. M. Zhao, L. H. Liu, and M. Antezza, Radiative heat transfer between metallic nanoparticle clusters in both near field and far field, Phys. Rev. B **99**, 134207 (2019).

[34] D. Xu, J. Zhao, and L. Liu, Near-field thermal radiation of gradient refractive index slab: Internal polaritons, Appl. Phys. Lett. **119**, 141106 (2021).

[35] A. Ott, S.-A. Biehs, and P. Ben-Abdallah, Anomalous photon thermal Hall effect, Phys. Rev. B **101**, 241411(R) (2020).

[36] S. A. Biehs, R. S. Messina, P. Venkataram, A. W. Rodriguez, J. C. Cuevas, and P. Ben-Abdallah, Near-field radiative heat transfer in many-body systems, Rev. Mod. Phys. **93**, 025009 (2021).

[37] K. Z. Shi, Z. Y. Chen, X. N. Xu, J. Evans, and S. L. He, Optimized colossal near-field thermal radiation enabled by manipulating coupled plasmon polariton geometry, Adv. Mater. **33**, 2106097 (2021).

[38] K. Z. Shi, R. Liao, G. J. Cao, F. L. Bao, and S. L. He, Enhancing thermal radiation by graphene-assisted hBN/SiO_2 hybrid structures at the nanoscale, Opt. Express **26**, A591 (2018).

[39] K. Z. Shi, Z. Y. Chen, Y. X. Xing, J. X. Yang, X. N. Xu, S. Evans, and S. L. He, Near-field radiative heat transfer modulation with an ultrahigh dynamic range through mode mismatching, Nano Lett. **22**, 7753 (2022).

[40] K. Z. Shi, Y. C. Sun, Z. Y. Chen, N. He, F. L. Bao, J. Evans, and S. L. He, Colossal enhancement of near-field thermal radiation across hundreds of nanometers between millimeter-scale plates through surface plasmon and phonon polaritons coupling, Nano Lett. **19**, 8082 (2019).

[41] K. Z. Shi, F. L. Bao, and S. L. He, Enhanced near-field thermal radiation based on multilayer graphene-hBN heterostructures, ACS Photonics **4**, 971 (2017).

[42] K. Z. Shi, F. L. Bao, N. He, and S. L. He, Near-field heat transfer between graphene-Si grating heterostructures with multiple magnetic-polaritons coupling, Int. J. Heat Mass Transfer **134**, 1119 (2019).

[43] M. J. He, H. Qi, Y. T. Ren, Y. J. Zhao, and M. Antezza, Magnetoplasmonic manipulation of nanoscale thermal radiation using twisted graphene gratings, Int. J. Heat Mass Transfer **150**, 119305 (2020).

[44] M. J. He, H. Qi, Y. T. Ren, Y. J. Zhao, and M. Antezza, Graphene-based thermal repeater, Appl. Phys. Lett. **115**, 263101 (2019).

[45] Y. Zhang, H. L. Yi, H. P. Tan, and M. Antezza, Giant resonant radiative heat transfer between nanoparticles, Phys. Rev. B **100**, 134305 (2019).

[46] Y. Zhang, M. Antezza, H. L. Yi, and H. P. Tan, Metasurface-mediated anisotropic radiative heat transfer between nanoparticles, Phys. Rev. B **100**, 085426 (2019).

[47] Z. H. Zheng, X. L. Liu, A. Wang, and Y. M. Xuan, Graphene-assisted near-field radiative thermal rectifier based on phase transition of vanadium dioxide (VO_2), Int. J. Heat Mass Transfer **109**, 63 (2017).

[48] E. Moncada-Villa and J. Cuevas, Normal-Metal–Superconductor Near-Field Thermal Diodes and Transistors, Phys. Rev. Appl. **15**, 024036 (2021).

[49] Y. Liu, Y. P. Tian, F. Q. Chen, A. Caratenuto, X. J. Liu, M. Antezza, and Y. Zheng, Ultrahigh-rectification near-field radiative thermal diode using infrared-transparent film backsided phase-transition metasurface, Appl. Phys. Lett. **119**, 123101 (2021).

[50] P. Doyeux, S. Gangaraj, G. Hanson, and M. Antezza, Giant Interatomic Energy-Transport Amplification with Nonreciprocal Photonic Topological Insulators, Phys. Rev. Lett. **119**, 173901 (2017).

[51] A. Ott, R. Messina, P. Ben-Abdallah, and S. A. Biehs, Radiative thermal diode driven by nonreciprocal surface waves, Appl. Phys. Lett. **114**, 163105 (2019).

[52] B. Zhao, C. Guo, C. A. C. Garcia, P. Narang, and S. H. Fan, Axion-field-enabled nonreciprocal thermal radiation in Weyl semimetals, Nano Lett. **20**, 1923 (2020).

[53] C. Guo, B. Zhao, D. Huang, and S. H. Fan, Radiative thermal router based on tunable magnetic Weyl semimetals, ACS Photonics **7**, 3257 (2020).

[54] J. Z. Wu, H. T. Li, C. J. Fu, and X. H. Wu, High quality factor nonreciprocal thermal radiation in a Weyl semimetal film via the strong coupling between Tamm plasmon and defect mode, Int. J. Therm. Sci. **184**, 107902 (2023).

[55] Y. S. Sun, Y. Hu, K. Z. Shi, J. H. Zhang, D. D. Feng, and X. H. Wu, Negative differential thermal conductance between Weyl semimetals nanoparticles through vacuum, Phys. Scr. **97**, 095506 (2022).

[56] Z. M. Zhang and L. X. Zhu, Nonreciprocal Thermal Photonics for Energy Conversion and Radiative Heat Transfer, Phys. Rev. Appl. **18**, 027001 (2022).

[57] J. Wu, B. Y. Wu, Z. M. Wang, and X. H. Wu, Strong nonreciprocal thermal radiation in Weyl semimetal-dielectric multilayer structure, Int. J. Therm. Sci. **181**, 107788 (2022).

[58] B. Zhao, J. H. Wang, Z. X. Zhao, C. Guo, Z. F. Yu, and S. H. Fan, Nonreciprocal Thermal Emitters using Metasurfaces with Multiple Diffraction Channels, Phys. Rev. Appl. **16**, 064001 (2021).

[59] X. H. Wu, H. Y. Yu, F. Wu, and B. Y. Wu, Enhanced nonreciprocal radiation in Weyl semimetals by attenuated total reflection, AIP Adv. **11**, 075106 (2021).

[60] G. M. Tang, J. Chen, and L. Zhang, Twist-induced control of near-field heat radiation between magnetic Weyl semimetals, ACS Photonics **8**, 443 (2021).

[61] N. Armitage, E. Mele, and A. Vishwanath, Weyl and Dirac semimetals in three-dimensional solids, Rev. Mod. Phys. **90**, 015001 (2018).

[62] Z. Yu, X. Li, T. Lee, and H. Iizuka, Near-field radiative heat transfer between Weyl semimetal multilayers, Int. J. Heat Mass Transfer **197**, 123339 (2022).

[63] G. D. Xu, J. Sun, and H. M. Mao, Near-field radiative thermal modulation between Weyl semimetal slabs, J. Quant. Spectrosc. Radiat. Transfer **253**, 107173 (2020).

[64] Z. Q. Yu, X. P. Li, T. Lee, and H. Iizuka, Near-field radiative heat transfer in three-body Weyl semimetals, Opt. Express **30**, 31584 (2022).

[65] X. H. Wu, C. J. Fu, and Z. M. Zhang, Influence of hBN orientation on the near-field radiative heat transfer between graphene/hBN heterostructures, J. Photonics Energy **9**, 032702 (2018).

[66] R. Messina, M. Tschikin, S. A. Biehs, and P. Ben-Abdallah, Fluctuation-electrodynamic theory and dynamics of heat transfer in systems of multiple dipoles, Phys. Rev. B **88**, 104307 (2013).

[67] P. Ben-Abdallah, S. A. Biehs, and K. Joulain, Many-Body Radiative Heat Transfer Theory, Phys. Rev. Lett. **107**, 114301 (2011).

[68] J.-R. Soh, F. De Juan, M. G. Vergniory, N. B. M. Schröter, M. C. Rahn, D. Y. Yan, J. Jiang, M. Bristow, P. Reiss, J. N. Blandy *et al.*, Ideal Weyl semimetal induced by magnetic exchange, Phys. Rev. B **100**, 201102(R) (2019).

[69] V. Asadchy, C. Guo, B. Zhao, and S. H. Fan, Sub-wavelength passive optical isolators using photonic structures based on Weyl semimetals, Adv. Opt. Mater. **8**, 2000100 (2020).

[70] K. Wang and L. Gao, High-efficient photonic thermal rectification with magnetocontrollability, ES Energy Environ. **7**, 12 (2019).

[71] A. Ott and S. A. Biehs, Thermal rectification and spin-spin coupling of nonreciprocal localized and surface modes, Phys. Rev. B **101**, 155428 (2020).

[72] A. Manjavacas and F. Abajo, Radiative heat transfer between neighboring particles, Phys. Rev. B **86**, 075466 (2012).

[73] R. Ekeroth, A. García-Martín, and J. Cuevas, Thermal discrete dipole approximation for the description of thermal emission and radiative heat transfer of magneto-optical systems, Phys. Rev. B **95**, 235428 (2017).

[74] S. Albaladejo, R. Gómez-Medina, L. Froufe-Pérez, H. Marinchio, R. Carminati, J. Torrado, G. Armelles, A. García-Martín, and J. Sáenz, Radiative corrections to the polarizability tensor of an electrically small anisotropic dielectric particle, Opt. Express **18**, 3556 (2010).

[75] J. Dong, J. M. Zhao, and L. H. Liu, Long-distance near-field energy transport via propagating surface waves, Phys. Rev. B **97**, 075422 (2018).

[76] Y. Zhang, C. L. Zhou, H. L. Yi, and H. P. Tan, Radiative Thermal Diode Mediated by Nonreciprocal Graphene Plasmon Waveguides, Phys. Rev. Appl. **13**, 034021 (2020).

[77] Y. Yang, S. Basu, and L. P. Wang, Radiation-based near-field thermal rectification with phase transition materials, Appl. Phys. Lett. **103**, 163101 (2013).

[78] M. Q. Yuan, Y. Zhang, S. H. Yang, C. L. Zhou, and H. L. Yi, Near-field thermal rectification driven by nonreciprocal hyperbolic surface plasmons, Int. J. Heat Mass Transfer **185**, 122437 (2022).

[79] R. J. William, Transient shutdown analysis of low-temperature thermal diodes, NASA Technical Paper No. 1369, NASA Ames Research Center Moffett Field, CA, United States, 1979.

[80] R. Williams, Investigation of a cryogenic thermal diode, in *Proceedings of 3rd International Heat Pipe Conference* (AIAA, Reston, VA, 1978).

[81] G. T. Colwell, Prediction of cryogenic heat pipes performances, Technical Rep. No. NASA-CR-146510, Georgia Inst. of Tech. Atlanta, GA, United States, 1976.

[82] A. Ott, P. Ben-Abdallah, and S. A. Biehs, Circular heat and momentum flux radiated by magneto-optical nanoparticles, Phys. Rev. B **97**, 205414 (2018).

[83] I. Latella and P. Ben-Abdallah, Giant Thermal Magnetoresistance in Plasmonic Structures, Phys. Rev. Lett. **118**, 173902 (2017).

[84] R. Ekeroth, P. Ben-Abdallah, J. Cuevas, and A. García-Martín, Anisotropic thermal magnetoresistance for an active control of radiative heat transfer, ACS Photonics **5**, 705 (2018).

[85] P. Ben-Abdallah, Photon Thermal Hall Effect, Phys. Rev. Lett. **116**, 084301 (2016).

[86] R. Messina, S. A. Biehs, and P. Ben-Abdallah, Surface-mode-assisted amplification of radiative heat transfer between nanoparticles, Phys. Rev. B **97**, 165437 (2018).

[87] K. Joulain, J. P. Mulet, F. Marquier, R. Carminati, and J. J. Greffet, Surface electromagnetic waves thermally excited: Radiative heat transfer, coherence properties and Casimir forces revisited in the near field, Surf. Sci. Rep. **57**, 59 (2005).

[88] P. Ben-Abdallah, Multitip Near-Field Scanning Thermal Microscopy, Phys. Rev. Lett. **123**, 264301 (2019).

[89] D. Thompson, L. X. Zhu, E. Meyhofer, and P. Reddy, Nanoscale radiative thermal switching via multi-body effects, Nat. Nanotechnol. **15**, 99 (2020).